The structural and magnetic characterization of 6H-perovskite-type oxides $Ba_3LnIr_2O_9$ (Ln = Y, lanthanides)

2004 J. Phys.: Condens. Matter 16 2849

(http://iopscience.iop.org/0953-8984/16/16/009)

INSTITUTE OF PHYSICS PUBLISHING JOURNAL OF PHYSICS: CONDENSED MATTER

J. Phys.: Condens. Matter **16** (2004) 2849–2860 PII: S0953-8984(04)73705-4

The structural and magnetic characterization of 6H-perovskite-type oxides $Ba_3LnIr_2O_9$ (Ln = Y, lanthanides)

Yoshihiro Doi and Yukio Hinatsu

Division of Chemistry, Graduate School of Science, Hokkaido University, Sapporo 060-0810, Japan

Received 18 December 2003
Published 8 April 2004
Online at stacks.iop.org/JPhysCM/16/2849
DOI: 10.1088/0953-8984/16/16/009

Abstract

The crystal structures and magnetic properties of quaternary oxides $Ba_3LnIr_2O_9$ (Ln = Y, lanthanides) are reported. Rietveld analyses of their x-ray diffraction data indicate that they adopt the 6H-perovskite-type structure with space group $P6_3/mmc$ or, in the case of Ln = La and Nd only, a monoclinically distorted structure with space group $C2/c$. They have the valence state of $Ba_3Ln^{4+}Ir_2^{4+}O_9$ (for Ln = Ce, Pr, and Tb) or $Ba_3Ln^{3+}Ir_2^{4.5+}O_9$ (for Ln = Y and other lanthanides). Measurements of the magnetic susceptibility and specific heat were carried out for Ln = Y, Ce, Pr, Tb, and Lu. It was found that the effective magnetic moment of Ir ions is significantly small, which indicates the existence of the strong antiferromagnetic interaction between Ir ions in the Ir_2O_9 bioctahedra. The Y and Lu compounds with an unpaired magnetic moment remaining in the $Ir_2^{4.5+}O_9$ show an antiferromagnetic transition at 4.0 and 5.1 K, respectively. For $Ba_3TbIr_2O_9$, a long-range magnetic ordering of Tb^{4+} ions was found at 2.0 K.

1. Introduction

Perovskites or perovskite-related oxides containing platinum group metals often exhibit interesting magnetic and electrical properties: for example, Sr_2RuO_4 (superconductivity below ∼1 K) [1], $SrRuO_3$ (ferromagnetic below 160 K) [2], Sr_2IrO_4 (weak ferromagnetic below 250 K) [3], etc. The quaternary oxides $Ba_3MRu_2O_9$ (M = alkali, alkaline earth, 3d transition metal elements, etc) also show interesting magnetic properties [4–7]. Many of them adopt the 6H-$BaTiO_3$ structure [8], in which the Ru and M ions occupy the face-sharing octahedral sites (Ru_2O_9 dimer) and the corner-sharing octahedral ones (MO_6 octahedron), respectively. This structure has a short Ru–Ru distance (2.5–2.8 Å) in the Ru_2O_9 dimer, thus strong magnetic interaction exists between Ru ions. This magnetic interaction often brings about the antiferromagnetic spin-pairing of Ru ions [4].

Recently, we have reported the magnetic properties of the 6H-perovskites $Ba_3LnRu_2O_9$ (Ln = Y, lanthanides) [9–12]. They adopt the valence configurations of $Ba_3Ln^{3+}Ru_2^{4.5+}O_9$

(for Ln = Y, La, Nd, Sm–Gd, Dy–Lu) [9, 10, 12–15] or $Ba_3Ln^{4+}Ru_2^{4+}O_9$ (for Ln = Ce, Pr, and Tb) [11, 15]. These compounds show a characteristic temperature dependence of the magnetic susceptibilities; that is, a broad maximum at 135–400 K and a magnetic transition at 4.5–24 K [9–12]. These magnetic properties mainly reflect two kinds of magnetic interactions: the interaction between Ru ions in the Ru_2O_9 dimer and that between Ln and Ru ions.

We now turn our attention to the magnetic properties of the iridium-based oxides $Ba_3LnIr_2O_9$. Their crystal structures were reported for Ln = Y, La, Nd, Sm–Gd, Dy, Ho, and Yb [16]; they adopt 6H-perovskite-type structures in analogy with $Ba_3LnRu_2O_9$. The Ir and Ru ions often produce oxides with common crystal structures; however, their physical properties are remarkably different (e.g. Sr_2RuO_4 [1] and Sr_2IrO_4 [3]). Such differences provide us with a significant motivation for investigating the effects of Ru substitution for Ir in the face-sharing octahedral sites. Before now, the magnetic properties of $Ba_3LnIr_2O_9$ were unknown apart from the magnetic susceptibility of $Ba_3YIr_2O_9$ [17]. In this study, we investigated the magnetic properties of $Ba_3LnIr_2O_9$ (Ln = Y, Ce, Pr, Tb, and Lu). The results of their electrical resistivity, magnetic susceptibility, and specific heat measurements are reported. In addition, we completed the structural data for this series of compounds including previously unreported materials (Ln = Ce, Pr, Tb, Er, Tm, Lu) by x-ray diffraction measurements.

2. Experimental details

Polycrystalline samples of $Ba_3LnIr_2O_9$ (Ln = Y, La–Nd, Sm–Lu) were synthesized by conventional solid-state reaction. As starting materials, $BaCO_3$ and Ln_2O_3, CeO_2, Pr_6O_{11}, Tb_4O_7, and Ir powders were used. Before use, La_2O_3 and Nd_2O_3 were dried in air at 900 °C for a day. Stoichiometric amounts of them were mixed in an agate mortar. The mixtures were pressed into pellets and then calcined at 900 °C for 12 h. The calcined materials were fired in air at 1100–1300 °C for 72–144 h with several intermediate grindings and pelletings.

The x-ray diffraction measurements were taken at room temperature in the range $10° \leqslant 2\theta \leqslant 120°$ using a 2θ step size of 0.02° with Cu Kα radiation on a Rigaku MultiFlex diffractometer. The data were analysed by the Rietveld technique, using the program RIETAN2000 [18].

The magnetic measurements were carried out using a SQUID magnetometer (Quantum Design, MPMS-5S). The temperature dependence of the magnetic susceptibilities was measured under both zero-field-cooled (ZFC) and field-cooled (FC) conditions in an applied field of 0.1 T over the temperature range 1.8–400 K. For $Ba_3TbIr_2O_9$, the field dependence of the magnetization was measured between 0 and 5 T.

Specific heat measurements were performed using a relaxation technique with a commercial physical property measurement system (Quantum Design, PPMS model) in the temperature range 1.8–300 K. The sintered sample in the form of a pellet was mounted on a thin alumina plate with grease for better thermal contact.

The temperature dependence of the resistivity was measured in the temperature range 100–400 K using a DC four-probe technique with the PPMS. The sintered samples were cut into pieces having sizes of approximately 5.0 × 2.5 × 1.0 mm^3. Four contact wires were painted onto the samples using silver paste.

3. Results and discussion

3.1. The crystal structures of $Ba_3LnIr_2O_9$

The $Ba_3LnIr_2O_9$ prepared in this study crystallize as 6H-perovskite or its related structure. The x-ray diffraction profiles for $Ba_3LaIr_2O_9$ and $Ba_3LuIr_2O_9$ are shown in figure 1. The

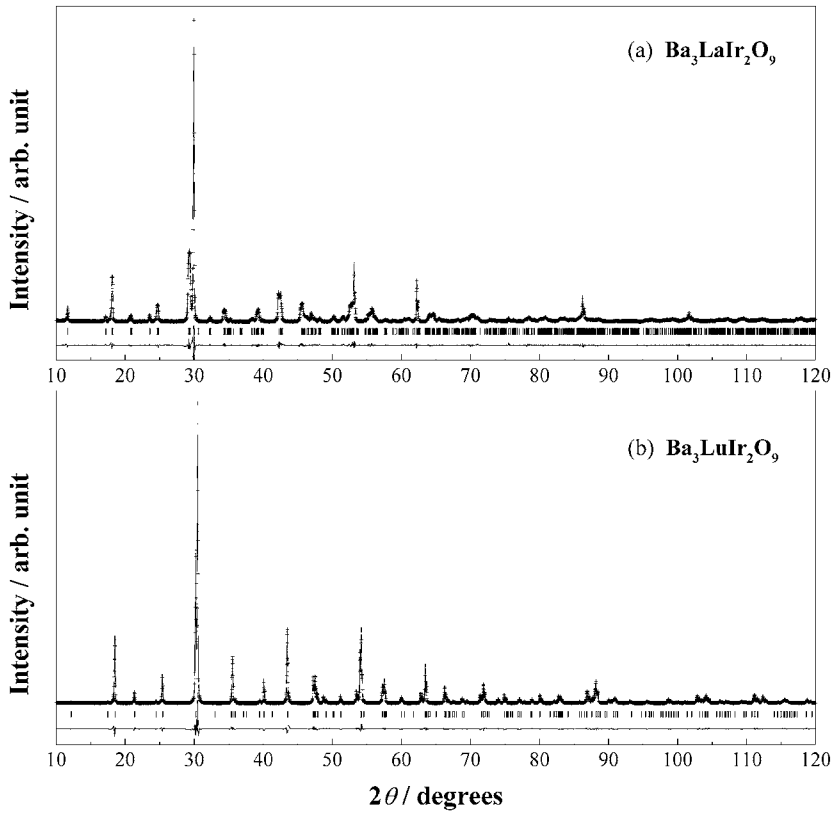

Figure 1. X-ray diffraction profiles for (a) $Ba_3LaIr_2O_9$ and (b) $Ba_3LuIr_2O_9$.

diffraction data for compounds with Ln = Y, Ce, Pr, Sm–Lu were indexed in a hexagonal unit cell with space group $P6_3/mmc$, while those for compounds with Ln = La and Nd were indexed in a monoclinic unit cell with space group $C2/c$ ($a_{mono} \sim a_{hex}$, $b_{mono} \sim \sqrt{3}a_{hex}$, $c_{mono} \sim c_{hex}$, $\beta_{mono} \sim 90°$). The schematic structure of $Ba_3LnIr_2O_9$ is illustrated in figure 2. Both structures have two kinds of octahedral site: corner-sharing and face-sharing. The Ln and Ir ions occupy the former and latter sites, respectively.

The lattice parameters and reliability factors for $Ba_3LnIr_2O_9$ and the structural parameters for Ln = La and Lu are listed in tables 1 and 2, respectively. The lattice parameters for Ln = Y, La, Nd, Sm–Gd, Dy, Ho, and Yb show good agreement with those in the previous report [16]; thus it is likely that our samples also have a valence configuration of $Ba_3Ln^{3+}Ir_2^{4.5+}O_9$. The variation of lattice parameters for $Ba_3LnIr_2O_9$ with the ionic radius of Ln^{3+} is shown in figure 3. For comparison, the lattice parameters for Ru-analogues $Ba_3LnRu_2O_9$ are also plotted. The lattice parameters increase monotonically with the ionic radius of Ln^{3+} except for Ln = Ce, Pr, and Tb. The variation of the Ln–O(2) length is plotted in figure 4(a). For only these three compounds, the Ln–O(2) lengths are much shorter than those for the $Ba_3Ln^{3+}Ir_2^{4.5+}O_9$ compounds. These facts indicate that the Ln ion is in the tetravalent state (i.e., $Ba_3Ln^{4+}Ir_2^{4+}O_9$). This result is the same as that found in the $Ba_3LnRu_2O_9$ [11].

The variation of the Ir–Ir distance in the Ir_2O_9 dimer is plotted in figure 4(b). The $Ba_3LnIr_2O_9$ compounds have a short Ir–Ir distance (2.53–2.58 Å), which is comparable to the Ru–Ru distance of the 6H-perovskites $Ba_3MRu_2O_9$ (M = alkali, alkaline earth,

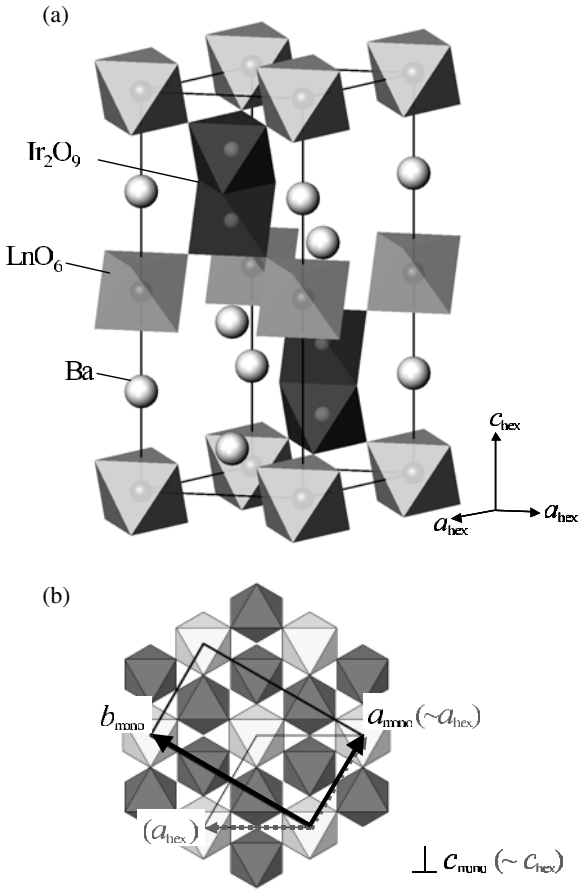

Figure 2. (a) The crystal structure of hexagonal $Ba_3LnIr_2O_9$. (b) A schematic illustration of the relationship of the unit cell axes between the hexagonal (dotted arrows) and monoclinic (solid arrows) cells.

lanthanides, transition metal elements, etc). For the Ru compounds, it is known that this distance increases with increasing the average Ru valence due to the electrostatic repulsion between Ru ions [7]. Typical Ru–Ru distances are 2.48–2.49 Å (for Ru^{4+}) [10, 15], 2.52–2.58 Å ($Ru^{4.5+}$) [9, 11, 12, 14, 15, 19], 2.65–2.70 Å (Ru^{5+}) [4, 6, 19–21], and 2.75–2.77 Å ($Ru^{5.5+}$) [7]. Although such a tendency is not clear between $Ba_3Ln^{3+}Ir_2^{4.5+}O_9$ (2.54–2.58 Å) and $Ba_3Ln^{4+}Ir_2^{4+}O_9$ (2.53–2.57 Å), the effect of the electrostatic repulsion appears in the centre-shift (Δ) of the Ir position in the IrO_6 octahedron (figure 4(c)). Here, the centre is defined as a 4f position (Wyckoff's crystallographic site in the hexagonal cell) at which six Ir–O bonds are equal in lengths. A positive Δ value represents the situation that Ir ions in the Ir_2O_9 dimer keep away from each other. The Δ value for $Ba_3Ln^{3+}Ir_2^{4.5+}O_9$ (0.07–0.13 Å) is much larger than that for $Ba_3Ln^{4+}Ir_2^{4+}O_9$ (0.03–0.05 Å); this result reflects the stronger electrostatic repulsion between Ir ions in the former compounds than that in the latter compounds.

3.2. Electrical resistivity

The resistivity of $Ba_3LnIr_2O_9$ (Ln = Pr, Nd, and Sm) is plotted as a function of reciprocal temperature in figure 5. They are nonmetallic at least in the range 120–400 K, showing an

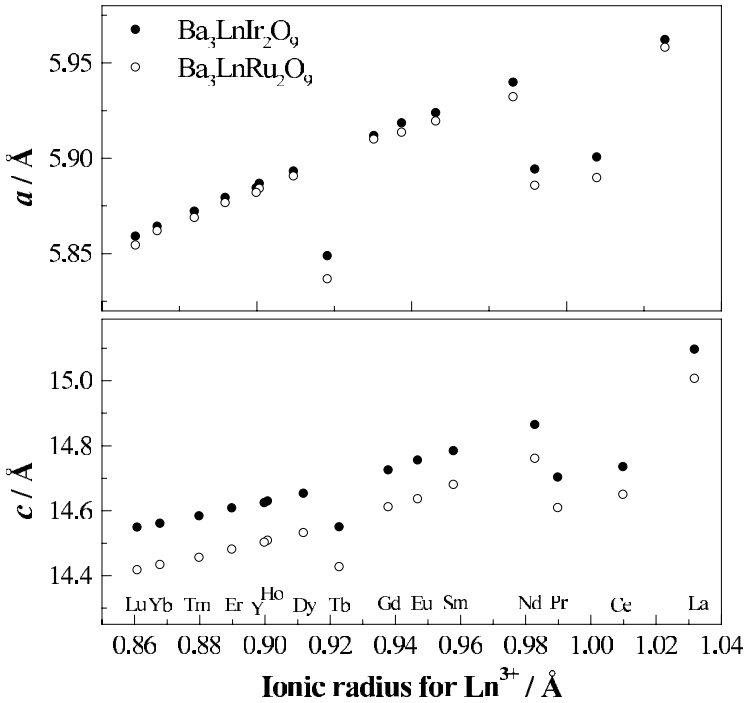

Figure 3. The variation of the lattice parameters for $Ba_3LnIr_2O_9$ and $Ba_3LnRu_2O_9$ (see [8–11]). Note that a_{mono} and c_{mono} are plotted for the monoclinic $Ba_3LaIr_2O_9$ and $Ba_3NdIr_2O_9$.

Table 1. Lattice parameters and reliability factors for $Ba_3LnIr_2O_9$. (Note: space group $P6_3/mmc$; $z = 2$. Definitions of the reliability factors R_{wp}, R_I and R_e are as follows: $R_{wp} = [\sum w(|F_o| - |F_c|)^2 / \sum w|F_o|^2]^{1/2}$, $R_I = \sum |I_{ko} - I_{kc}| / \sum I_{ko}$, $R_e = [(N - p) / \sum_i w_i y_i^2]^{1/2}$).

Ln	a (Å)	b (Å)	c (Å)	β (deg)	R_{wp} (%)	R_I (%)	R_e (%)
Y	5.8842(2)		14.6224(3)		12.21	2.84	8.03
La[a]	5.9628(2)	10.3244(3)	15.0953(6)	90.622(2)	11.39	1.59	7.94
Ce	5.9002(1)		14.7333(3)		12.00	1.91	8.73
Pr	5.8939(2)		14.7014(4)		12.22	1.86	9.42
Nd[a]	5.9395(2)	10.2844(3)	14.8635(7)	90.567(2)	11.64	1.85	8.05
Sm	5.9235(2)		14.7828(4)		11.70	2.05	7.41
Eu	5.9182(1)		14.7542(3)		11.87	2.17	7.39
Gd	5.9115(1)		14.7238(3)		12.90	2.93	7.25
Tb	5.8486(1)		14.5482(2)		11.81	1.67	8.99
Dy	5.8930(2)		14.6514(4)		12.00	2.39	7.16
Ho	5.8864(1)		14.6280(2)		12.58	3.13	6.70
Er	5.8791(1)		14.6067(3)		11.27	2.74	6.70
Tm	5.8719(1)		14.5820(3)		10.24	1.88	6.53
Yb	5.8640(1)		14.5595(3)		11.45	2.55	6.60
Lu	5.8587(1)		14.5471(3)		10.89	2.13	6.53

[a] Monoclinic structure with space group $C2/c$ ($z = 4$).

increase of resistivity with decreasing temperature. A significant difference in the behaviour of the resistivity was not observed in three compounds: hexagonal $Ba_3Pr^{4+}Ir_2^{4+}O_9$, monoclinic $Ba_3Nd^{3+}Ir_2^{4.5+}O_9$, and hexagonal $Ba_3Sm^{3+}Ir_2^{4.5+}O_9$.

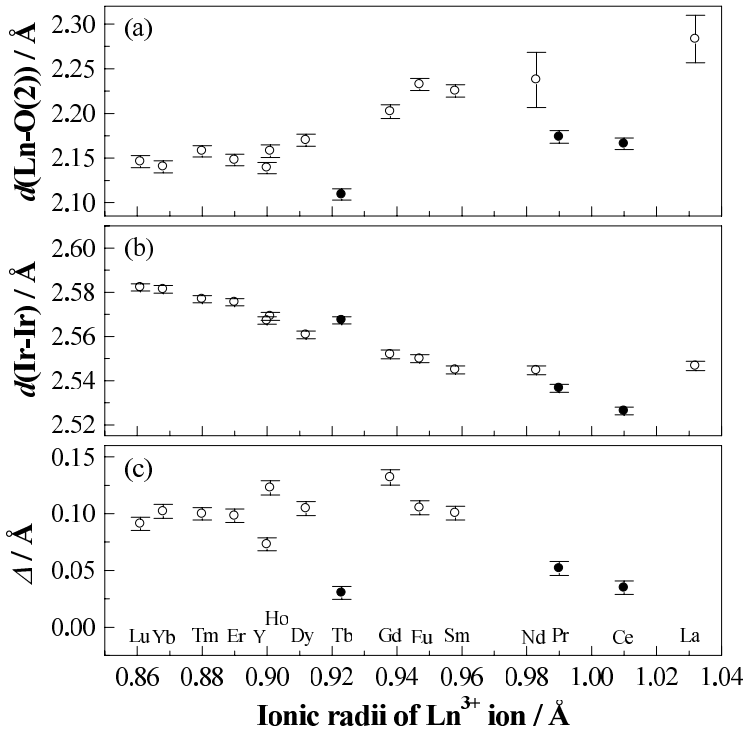

Figure 4. The variation of (a) the Ln–O(2) length, (b) the Ir–Ir length, and (c) the centre-shift (Δ) of the Ir position in the IrO_6 octahedron. In the Δ plot, a positive value represents the situation that Ir ions in the Ir_2O_9 dimer keep away from each other.

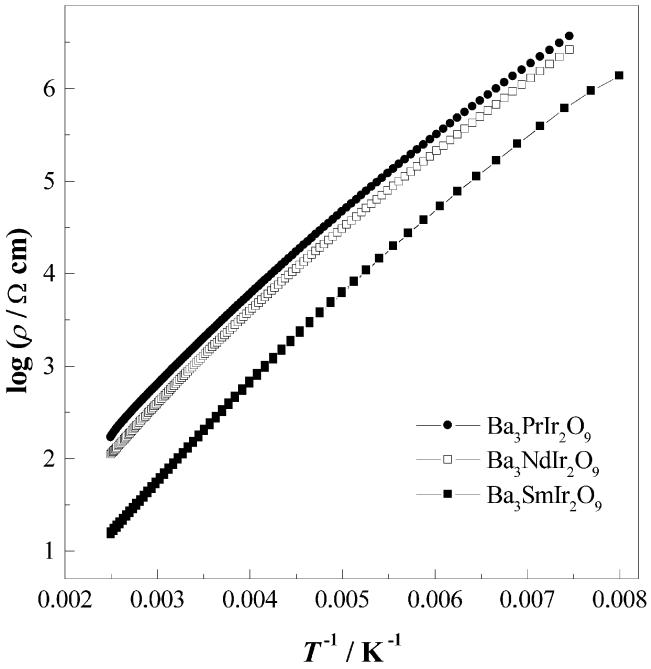

Figure 5. The temperature dependence of the resistivity for $Ba_3LnIr_2O_9$ (Ln = Pr, Nd, and Sm).

Table 2. Structural parameters for $Ba_3LaIr_2O_9$ and $Ba_3LuIr_2O_9$.

Atom	Site	x	y	z	B (Å^2)
$Ba_3LaIr_2O_9$ Space group $C2/c$ (No. 15), $z = 4$, $a = 5.9628(2)$ Å, $b = 10.3244(3)$ Å, $c = 15.0953(6)$ Å, $\beta = 90.622(2)°$					
Ba(1)	4e	0	−0.0012(6)	1/4	0.65(3)
Ba(2)	8f	0.0034(3)	0.3314(5)	0.1029(1)	0.65
La	4a	0	0	0	0.20(3)
Ir	8f	0.0072(2)	0.3343(4)	0.8343(1)	0.16(3)
O(1)	4e	0	0.505(4)	1/4	1.5(2)
O(2)	8f	0.267(5)	0.246(3)	0.243(1)	1.5
O(3)	8f	0.019(5)	0.824(4)	0.094(2)	1.5
O(4)	8f	0.267(5)	0.093(3)	0.086(1)	1.5
O(5)	8f	0.754(6)	0.091(3)	0.096(1)	1.5
$Ba_3LuIr_2O_9$ Space group $P6_3/mmc$ (No. 194), $z = 2$, $a = 5.8587(1)$ Å, $c = 14.5471(3)$ Å					
Ba(1)	2b	0	0	1/4	0.37(5)
Ba(2)	4f	1/3	2/3	0.9080(1)	0.67(3)
Lu	2a	0	0	0	0.05(4)
Ir	4f	1/3	2/3	0.1613(1)	0.32(2)
O(1)	6h	0.4938(8)	0.9876	1/4	0.7(3)
O(2)	12k	0.1721(7)	0.3442	0.4142(4)	1.3(2)

3.3. Magnetic susceptibility and specific heat

3.3.1. $Ba_3CeIr_2O_9$. Figure 6 shows the temperature dependence of the ZFC magnetic susceptibilities for $Ba_3Ce^{4+}Ir_2^{4+}O_9$. The FC data agree with the ZFC data over the whole experimental temperature range. The magnetic susceptibilities decrease monotonically with increasing temperature. In order to estimate the effective magnetic moment of Ir^{4+} ions (Ce^{4+} is nonmagnetic), the data were fitted using a modified Curie–Weiss law:

$$\chi = \frac{C}{T - \theta} + \chi_{\mathrm{TIP}}. \tag{1}$$

The effective magnetic moment (μ_{eff}), Weiss constant (θ), and temperature-independent paramagnetic susceptibility (χ_{TIP}) are 0.31(1) μ_{B} (=0.22 μ_{B}/Ir), −0.55(2) K, and 4.8(1) × 10^{-4} emu mol^{-1}, respectively. The temperature dependences of the magnetic susceptibility and specific heat divided by temperature at low temperatures are plotted in figures 7(a) and (b), respectively. This compound shows no anomaly down to 1.8 K.

The effective magnetic moment of $Ba_3CeIr_2O_9$ is excessively small compared with that expected for the free Ir^{4+} ion (1.73 μ_{B} for the low spin state). Even though we ignore the large χ_{TIP} in the fitting using equation (1), μ_{eff} is still small (0.78 μ_{B}/Ir at 300 K and 0.20 μ_{B}/Ir at 1.8 K). This indicates that the magnetic moments of Ir ions cancel each other in the Ir_2O_9 dimer, i.e., an antiferromagnetic spin-pairing of Ir^{4+} ions occurs. The antiferromagnetic interaction in the dimer has been found in many $Ba_3MRu_2O_9$ compounds with short Ru–Ru distances (2.48–2.77 Å) [4, 6, 7, 9–12]. Since $Ba_3CeIr_2O_9$ also has a short Ir–Ir distance (2.526(2) Å), it is likely that there exists a strong antiferromagnetic interaction between the Ir ions.

The origin of the Curie–Weiss-like behaviour of the magnetic susceptibility is not clear at present. In the antiferromagnetic dimer which consists of the same magnetic ions, its magnetic susceptibility ideally approaches zero with decreasing temperature, because such a dimer has

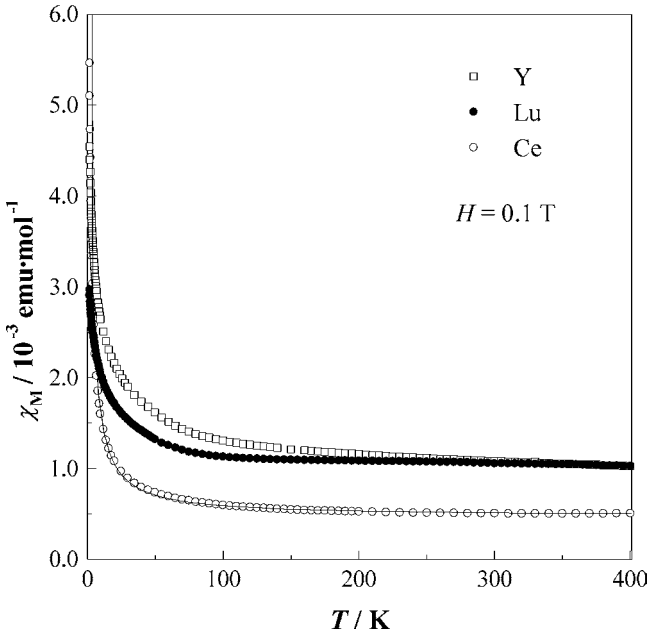

Figure 6. The temperature dependence of the magnetic susceptibility for $Ba_3LnIr_2O_9$ (Ln = Y, Ce, and Lu). The solid curve is the Curie–Weiss fitting for $Ba_3CeIr_2O_9$.

a singlet ($S = 0$) ground state. This may be due to the existence of magnetically unpaired Ir ions which are formed by the small amount of oxygen defects.

3.3.2. $Ba_3LnIr_2O_9$ (Ln = Y and Lu). The temperature dependences of the ZFC magnetic susceptibilities for $Ba_3Y^{3+}Ir_2^{4.5+}O_9$ and $Ba_3Lu^{3+}Ir_2^{4.5+}O_9$ are also shown in figure 6. Attempts to fit the Curie–Weiss law to their magnetic susceptibilities ended in poor results. For both compounds, the magnetic moments calculated from the data at 1.8 and 300 K are about 0.15 and 1.1 μ_B (per Ir ion), respectively. These magnetic moments are much smaller than the average magnetic moment (2.34 μ_B) which is expected from the spin-only values of Ir^{4+} and Ir^{5+} ions in the low-spin state. This result indicates the existence of a small magnetic moment remaining in the $Ir_2^{4.5+}O_9$ dimer. We consider that it is derived from an uncancelled magnetic moment in the antiferromagnetic $Ir_2^{4.5+}O_9$ dimer or the magnetic moment of the only Ir^{4+} ion. In the latter case, half of the iridium ion is in the pentavalent state and it is in a singlet ground state [22].

Figure 7(b) shows the temperature dependence of the specific heat divided by temperature (C_p/T). $Ba_3Y^{3+}Ir_2^{4.5+}O_9$ and $Ba_3Lu^{3+}Ir_2^{4.5+}O_9$ show a λ-type anomaly at 4.0 and 5.1 K, respectively. No such anomaly has been observed in the specific heat of $Ba_3Ce^{4+}Ir_2^{4+}O_9$. This result reflects the difference in the valency of Ir ions in the Ir_2O_9 dimer. At sufficiently low temperatures, the magnetic moment of the $Ir_2^{4+}O_9$ dimer should be almost cancelled ($S_{dimer} = 0$) by the strong Ir–Ir antiferromagnetic interaction, while a magnetic moment ($S_{dimer} = 1/2$) in the $Ir_2^{4.5+}O_9$ dimer can remain when this dimer adopts the valence configuration of $Ir^{4+}Ir^{5+}O_9$. Therefore, the observed specific heat anomalies may be due to the magnetic ordering of such remaining magnetic moments.

In order to estimate the magnetic entropy change (ΔS_m) of these anomalies, the magnetic entropy (S_m) was calculated by $S_m = \int C_m/T \, dT$. The magnetic specific heat C_m was obtained by subtracting the lattice and electronic specific heats from the observed specific heat. The lattice and electronic contributions were approximated by using the data of $Ba_3Ce^{4+}Ir_2^{4+}O_9$. The

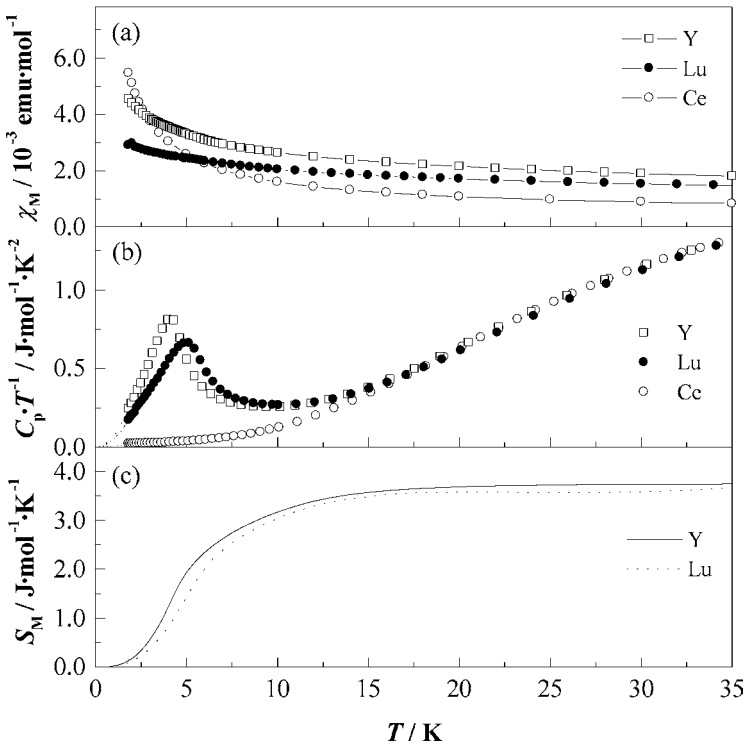

Figure 7. The temperature dependence of (a) the magnetic susceptibility, (b) the specific heat divided by temperature, and (c) the magnetic entropy for $Ba_3LnIr_2O_9$ (Ln = Y, Ce, and Lu). In (b), the dotted curves at low temperatures are extrapolated curves of $C_p/T \propto T^2$.

specific heat data below 1.8 K were estimated from the extrapolation curve of $C_p/T \propto T^2$ [23]. The temperature dependence of the magnetic entropy is shown in figure 7(c). The magnetic entropy changes for Y and Lu compounds are 3.6 and 3.7 J mol^{-1} K^{-1}, respectively. These values are very close to those found in $Ba_3M^{3+}Ru_2^{4.5+}O_9$ ($\Delta S_m \sim 3.0$ J mol^{-1} K^{-1}) with a nonmagnetic M^{3+} ion: M = Y, In, and Lu [11]. The observed magnetic entropy changes are smaller than the expected value of $R \ln(2S_{dimer}+1) = 5.76$ J mol^{-1} K^{-1}. This may be due to the occurrence of short-range magnetic ordering at higher temperatures.

3.3.3. $Ba_3LnIr_2O_9$ (Ln = Pr and Tb). The temperature dependences of the magnetic susceptibility and specific heat divided by temperature (C_p/T) for $Ba_3Pr^{4+}Ir_2^{4+}O_9$ are plotted in figures 8(a) and 9(b), respectively. The magnetic susceptibility of $Ba_3PrIr_2O_9$ shows no magnetic anomaly down to 1.8 K, and the C_p/T data only show a slight increase with decreasing temperature below ∼3 K. The susceptibility data in the high temperature region ($T > 100$ K) are fitted using the modified Curie–Weiss law. The effective magnetic moment and Weiss constant for $Ba_3PrIr_2O_9$ are obtained to be 0.75(1) μ_B and −5.3(7) K, respectively.

This effective magnetic moment is much smaller than the free-ion magnetic moments for Pr^{3+} (3.58 μ_B) and Pr^{4+} (2.54 μ_B) ions. It is close to the moments observed in perovskites containing the Pr^{4+} ion in the octahedral site: 0.68 μ_B for $BaPrO_3$ [24], 0.812–0.879 μ_B for $Ba_{1-x}Sr_xPrO_3$ [25], and 0.90 μ_B for $Ba_3PrRu_2O_9$ [11]. The small magnetic moments of $BaPrO_3$ and $Ba_{1-x}Sr_xPrO_3$ have been quantitatively analysed by the octahedral crystal field model using the g value of the electron paramagnetic resonance (EPR) spectrum of Pr^{4+} doped

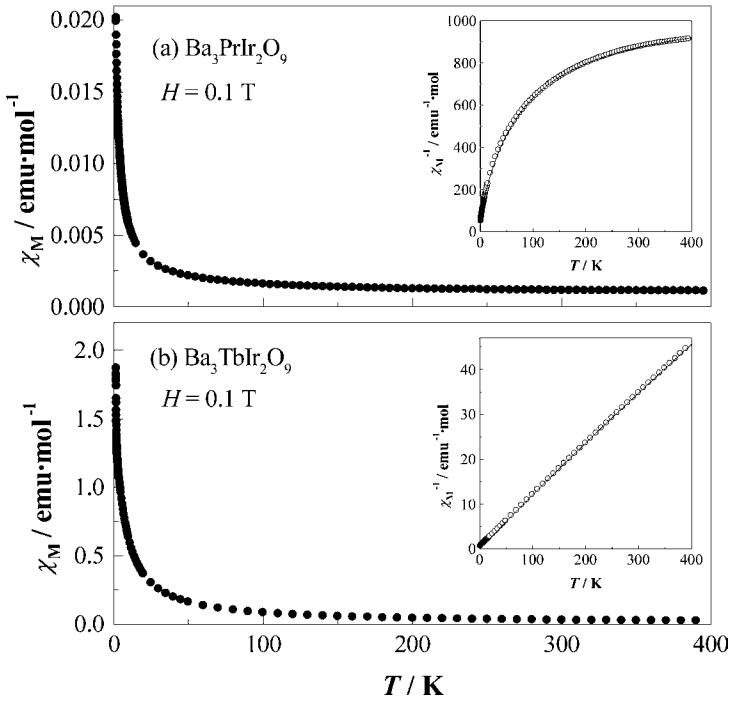

Figure 8. The temperature dependence of the magnetic susceptibility for $Ba_3LnIr_2O_9$ (Ln = Pr and Tb). The inset shows the reciprocal magnetic susceptibility (open circle) and the Curie–Weiss fitting (solid curve).

in diamagnetic $BaCeO_3$ and $Ba_{1-x}Sr_xCeO_3$ [25, 26]. The small magnetic moment found in $Ba_3PrIr_2O_9$ indicates that the Pr^{4+} ions are affected by the octahedral crystal field ($^2F_{5/2} \rightarrow \Gamma_7 + \Gamma_8$) and are probably in a Γ_7 ground state.

Figure 8(b) shows the magnetic susceptibility for $Ba_3Tb^{4+}Ir_2^{4+}O_9$ as a function of temperature. The Curie–Weiss fitting was carried out ($T > 100$ K); the effective magnetic moment and Weiss constant were obtained to be 8.10(1) μ_B and $-0.7(2)$ K, respectively. The effective magnetic moment of $Ba_3TbIr_2O_9$ is in good agreement with the free-ion magnetic moment for Tb^{4+} (7.94 μ_B) rather than that for Tb^{3+} (9.72 μ_B).

The temperature dependences of the magnetic susceptibility, specific heat divided by temperature, and magnetic entropy for $Ba_3TbIr_2O_9$ are shown in figure 9. Two specific heat anomalies have been found: a broad peak at 7.6 K and a sharp peak at 2.0 K. The magnetic entropy associated with the magnetic anomaly was estimated in the same manner as that used for the Y and Lu compounds. A large magnetic entropy change ($\sim$12.6 J mol^{-1} K^{-1}) associated with both anomalies is observed (figure 9(c)). This result indicates that these anomalies are attributed to the magnetic ordering of Tb^{4+} ions, because this value is comparable to that expected from $R\ln(2S + 1) = R\ln 8 = 17.3$ J mol^{-1} K^{-1} when the magnetic moments of $Tb^{4+}(4f^7)$ ions fully order.

We consider that the specific heat anomaly observed at 7.6 K actually begins below $\sim$24 K (see figure 9(b)). However, the magnetic susceptibility does not show any distinct magnetic anomaly around 7.6 or 24 K. This magnetic behaviour may be due to the short range magnetic ordering of Tb^{4+} ions. The specific heat anomaly at 2.0 K corresponds to a marked increase of the magnetic susceptibility at the same temperature. From measurements of the field dependence of the magnetization (figure 10), no magnetic hysteresis loop was found down

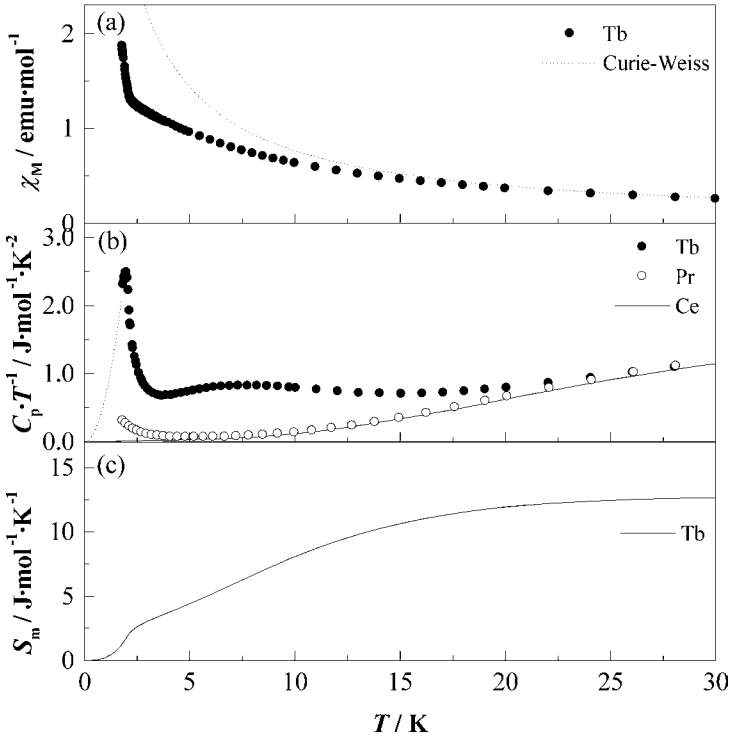

Figure 9. The temperature dependence of (a) the magnetic susceptibility for $Ba_3TbIr_2O_9$, (b) the specific heat divided by temperature for $Ba_3LnIr_2O_9$ (Ln = Ce, Pr, and Tb), and (c) the magnetic entropy for $Ba_3TbIr_2O_9$. In (b), the dotted curves at low temperatures are extrapolated curves of $C_p/T \propto T^2$.

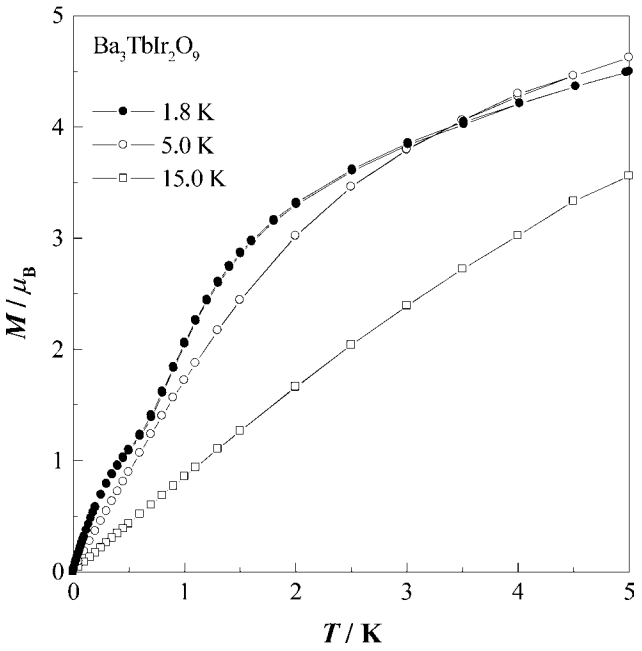

Figure 10. The field dependence of the magnetization for $Ba_3TbIr_2O_9$.

to 1.8 K. These results indicate that a long-range magnetic ordering of Tb^{4+} ions occurs at 2.0 K. The magnetization at 1.8 K shows a small anomaly at $H = 0.5$ T; however, its origin is unclear at present. In order to clarify the magnetic ordering of $Ba_3TbIr_2O_9$, detailed magnetic and neutron diffraction measurements at lower temperatures are needed.

4. Summary

The quaternary oxides $Ba_3LnIr_2O_9$ (Ln = Y, lanthanides) have the 6H-$BaTiO_3$-type structure. The structures of the La and Nd compounds are monoclinically distorted, while those of the others are hexagonal. The valence configuration at the B site is $Ba_3Ln^{3+}Ir_2^{4.5+}O_9$ except for Ln = Ce, Pr, and Tb. For the Ln = Ce, Pr, and Tb compounds, the Ln ions adopt the tetravalent state ($Ba_3Ln^{4+}Ir_2^{4+}O_9$). The Ir–Ir distance in the Ir_2O_9 dimer is short (2.53–2.58 Å). This short distance brings about a strong antiferromagnetic interaction between Ir ions. The results of the magnetic susceptibility and specific heat measurements indicate that there exists an antiferromagnetic pairing between Ir ions in the Ir_2O_9 dimer. In addition, magnetic anomalies due to the magnetic ordering of the unpaired magnetic moments of $Ir_2^{4.5+}O_9$ dimer or the magnetic moments of Ln ions have been observed.

Acknowledgment

The authors are indebted to the Japan Securities Scholarship Foundation for financial support.

References

[1] Maeno Y, Hashimoto H, Yoshida K, Nishizaki S, Fujita T, Bednorz J G and Lichtenberg F 1994 *Nature* **372** 532–4
[2] Callaghan A, Moeller C W and Ward R 1966 *Inorg. Chem.* **5** 1572–6
[3] Crawford M K, Subramanian M A, Harlow R L, Fernandez-Baca J A, Wang Z R and Johnston D C 1994 *Phys. Rev.* B **49** 9198–201
[4] Darriet J, Drillon M, Villeneuve G and Hagenmuller P 1976 *J. Solid State Chem.* **19** 213–20
[5] Rijssenbeek J T, Matl P, Batlogg B, Ong N P and Cava R J 1998 *Phys. Rev.* B **58** 10315–8
[6] Lightfoot P and Battle P D 1990 *J. Solid State Chem.* **89** 174–83
[7] Stitzer K E, Smith M D, Gemmill W R and zur Loye H-C 2002 *J. Am. Chem. Soc.* **124** 13877–85
[8] Burbank R D and Evans H T 1948 *Acta Crystallogr.* **1** 330–6
[9] Doi Y, Hinatsu Y, Shimojo Y and Ishii Y 2001 *J. Solid State Chem.* **161** 113–20
[10] Doi Y, Wakeshima M, Hinatsu Y, Tobo A, Ohoyama K and Yamaguchi Y 2001 *J. Mater. Chem.* **11** 3135–40
[11] Doi Y, Mastuhira K and Hinatsu Y 2002 *J. Solid State Chem.* **165** 317–23
[12] Doi Y and Hinatsu Y 2002 *J. Mater. Chem.* **12** 1792–5
[13] Treiber V U, Kemmler-Sack S, Ehmann A, Schaller H-U, Dürrschmidt E, Thumm I and Bader H 1981 *Z. Anorg. Allg. Chem.* **481** 143–52
[14] Rath M and Müller-Buschbaum Hk 1994 *J. Alloys Compounds* **210** 119–23
[15] Müller-Buschbaum Hk and Mertens B 1996 *Z. Naturf.* b **51** 79–84
[16] Thumm I, Treiber U and Kemmler-Sack S 1980 *J. Solid State Chem.* **35** 156–66
[17] Drillon M, Pourroy G and Darriet J 1984 *Chem. Phys.* **88** 27–37
[18] Izumi F and Ikeda T 2000 *Mater. Sci. Forum* **321–324** 198–203
[19] Rijssenbeek J T, Huang Q, Erwin R W, Zandbergen H W and Cava R J 1999 *J. Solid State Chem.* **146** 65–72
[20] Willkens J and Müller-Buschbaum Hk 1993 *Z. Anorg. Allg. Chem.* **619** 517–20
[21] Zandbergen H W and Ijdo D J W 1984 *Acta Crystallogr.* C **40** 919–22
[22] Wakeshima M, Harada D and Hinatsu Y 1999 *J. Alloys Compounds* **287** 130–6
[23] Joshua S J and Cracknell A P 1969 *Phys. Lett.* A **28** 562–3
[24] Hinatsu Y 1993 *J. Solid State Chem.* **102** 362–7
[25] Hinatsu Y 1995 *J. Solid State Chem.* **119** 405–11
[26] Hinatsu Y and Edelstein N 1994 *J. Solid State Chem.* **112** 53–7